Available online at www.sciencedirect.com
ScienceDirect
Journal of the Franklin Institute 347 (2010) 1353–1367
Journal of The Franklin Institute
www.elsevier.com/locate/jfranklin

Bifurcation analysis of a microcantilever in AFM system

Neng-Sheng Pai[a], Cheng-Chi Wang[b,*], David T.W. Lin[b]

[a]Department of Electrical Engineering, National Chin-Yi University of Technology, Taichung 411, Taiwan
[b]Graduate Institute of Mechatronic System Engineering, National University of Tainan, Tainan 700, Taiwan

Received 11 May 2009; accepted 10 June 2010

Abstract

The atomic force microscope system (AFM) has become a popular and useful instrument to measure the intermolecular forces with atomic resolution that can be applied in electronics, biological analysis, materials, semiconductors, etc. This paper studies the bifurcation phenomenon and complex nonlinear dynamic behavior of the probe tip between the sample and microcantilever of an atomic force microscope using the differential transformation method. The dynamic behavior of the probe tip is characterized with reference to bifurcation diagrams, phase portraits, power spectra, Poincaré maps, and maximum Lyapunov exponent plots produced using the time-series data obtained from differential transformation method. The results indicate that the probe tip behavior is significantly dependent on the magnitude of the vibrational amplitude. Specifically, the probe tip motion changes from T-periodic to 3T-periodic, then from 6T-periodic to multi-periodic, and finally to chaotic motion with windows of periodic motion as the vibrational amplitude is increased from 0 to 5.0. Furthermore, it is demonstrated that the differential transformation method is in good agreement for the considered system.

Keywords: Bifurcation; Microcandilever; AFM; Chaotic motion

1. Introduction

Recently, many significant researches have been studied to design, analyze, and implement micro- and nanosystems. The atomic force microscope (AFM) provides a

*Corresponding author.
E-mail address: wccpipn@yahoo.com.tw (C.-C. Wang).

0016-0032/$32.00 © 2010 The Franklin Institute. Published by Elsevier Ltd. All rights reserved.
doi:10.1016/j.jfranklin.2010.06.008

powerful tool for surface analysis applications in the nano-electronics and materials and biotechnology fields. Specifically, AFM-based system provides additional capabilities and is advantageous relative to other microscopic methods with regard to studies of surfaces and structures by providing reliable measurements at the nanoscale [1,2].

The nonlinear dynamic behavior of an AFM system between microcantilever and sample is a major concern since any irregular motion of the AFM probe tip inevitably degrades the precision of the measurement results. Burnham et al. [3] studied the dynamics of a microcantilever–sample interaction in AFM system experimentally and showed that the microcantilever performed chaotic motion under specific physical conditions. Ashhab et al. [4] modeled the microcantilever of an AFM using a single-frequency mode approximation and analyzed the chaotic dynamics of the cantilever–sample system using the Melnikov method. Sebastian et al. [5] predicted the behavior of the cantilever during tapping mode operation by a harmonic balancing and averaging technique. In addition, Basso et al. [6] utilized the Lennard–Jones potential within the dynamics for the AFM system and found the chaotic region of operation. Lee et al. [7] analyzed the effects of van der Waals and Derjaguin–Muller–Toporov forces on the tip–sample interactions induced in dynamic force microscopy (DFM). The authors also presented detailed experimental results, which provided valuable new perspectives and insights into DFM. Ruetzel et al. [8] applied the Galerkin method to investigate the nonlinear dynamics of an AFM probe tip under the assumption that the tip–surface interactions were governed by Lennard–Jones potentials. Based upon their analysis, the authors showed that the probe tip exhibited a broad range of dynamic phenomena, including both periodic and chaotic motion. However, chaotic behavior will cause the probe fatigued and then the controlling method is developed. In 2007, Yan et al. [9] designed variable structure control (VSC) for a chaotic symmetric gyro with linear-plus-cubic damping. The results show that the stable or unstable (chaotic) nonlinear gyros can be controlled and asymptotically driven by the system orbits to arbitrarily desired trajectories. Yau [10] presented a robust fuzzy sliding mode control (FSMC) scheme for the synchronization of two chaotic nonlinear gyros subject to uncertainties and external disturbances. The proposed scheme has a lower implementation cost and complexity.

None of the studies reviewed above presented phase portraits, power spectra, Poincaré maps, maximum Lyapunov exponent plots, or bifurcation diagrams to confirm the validity of their predictions for the AFM behavior or to clarify the origins of the chaotic motion observed in the AFM system. Accordingly, the present study investigates the dynamic behavior of an AFM probe tip using two numerical methods, namely the differential transformation method [11] and the Runge–Kutta method and then characterizes the dynamic response of the system with reference to phase portraits, power spectra, Poincaré maps, and maximum Lyapunov exponent plots. Finally, the onset of chaotic behavior in the AFM system is identified using bifurcation diagrams of the tip displacement and tip velocity, respectively, in which the amplitude of the probe tip vibration is taken as the bifurcation parameter.

The remainder of this paper is organized as follows. Section 2 presents a mathematical model for the relationship of the microcantilever tip and sample surface and describes the solution of this model using the differential transformation method. Section 3 compares and contrasts the numerical results obtained by the differential transformation method and the Runge–Kutta method for the dynamic response of the microcantilever tip at various vibrational amplitudes. Subsequently, the nonlinear dynamic behavior of the probe tip is

analyzed with reference to phase portraits, power spectra, Poincaré maps, maximum Lyapunov exponent plots, and bifurcation diagrams, respectively. Finally, Section 4 draws some brief conclusions.

2. Mathematical modeling

The behavior of an AFM microcantilever tip is modeled through a lumped-parameter's system approach as shown in Fig. 1. The cantilever is modeled as a spring-mass system which is excited by the motion of spring base. The dynamic behavior of this system can be represented in the following form [12,13]:

$$m_t \ddot{Y}(t) + c(\dot{Y}(t) - \dot{D}(t)) + k(Y(t) - D(t)) = Fv(t) \tag{1}$$

where $Y(t)$ and $D(t)$ denote the cantilever tip displacement and the base motion relative to the fixed base frame, respectively. m_t, c, and k are the cantilever tip mass, damping coefficient, and spring stiffness, respectively. $F_v(t)$ is the van der Waals force that is defined in the following form [13]:

$$F_v = \frac{C_H k}{(Z_b - Y)^2} - \frac{{R_m}^6 C_H k}{30(Z_b - Y)^8} \tag{2}$$

where Z_b denotes the distance from the sample to the fixed base frame, R_m denotes the molecular diameter, and the model parameter C_H is defined as $C_H = A_H R_t / 6k$ where A_H is the Hamaker constant and R_t the cantilever tip radius.

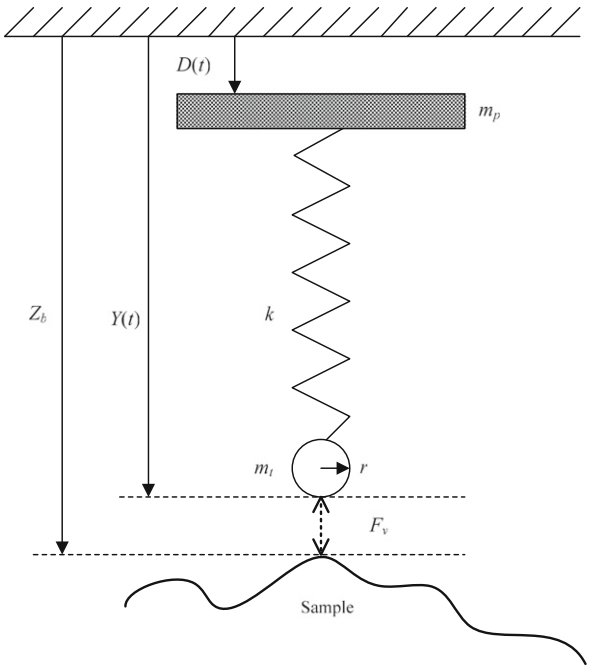

Fig. 1. AFM microcantilever tip model through a lumped-parameter's system.

The cantilever is driven through $D(t)$ as follows:

$$D(t) = A_d \sin(\omega t) \tag{3}$$

where A_d is the drive amplitude and ω the frequency. If $D(t)$ is replaced in cantilever–sample interaction Eq. (1), it yields

$$\ddot{Y}(t) + \frac{c}{m_t}\dot{Y}(t) - A_d\omega\frac{c}{m_t}\cos(\omega t) - \omega_t^2 A_d \sin(\omega t) + \omega_t^2 Y(t) = \frac{C_H\omega_t^2}{(Z_b - Y)^2} - \frac{R_m{}^6 C_H\omega_t^2}{30(Z_b - Y)^8} \tag{4}$$

where $\omega_t^2 = k/m_t$. The equations of motion in state-space form can now be presented as

$$Y_1(t) = Y(t), \quad Y_2(t) = \dot{Y}(t) \tag{5}$$

$$\dot{Y}_1(t) = Y_2(t) \tag{6}$$

$$\dot{Y}_2(t) = -\frac{c}{m_t}Y_2(t) + A_d\omega\frac{c}{m_t}\cos(\omega t) + A_d\omega_t^2\sin(\omega t) - \omega_t^2 Y_1(t) + \frac{C_H\omega_t^2}{(Z_b - Y_1)^2} - \frac{R_m{}^6 C_H\omega_t^2}{30(Z_b - Y_1)^8} \tag{7}$$

In order to express the equations of motion above in a non-dimensional form, the results in [14] are used with the critical value of $Y_s = 3/2(2C_H)^{1/3}$. Hence the system equations transfer to

$$\dot{X}_1 = X_2 \tag{8}$$

$$\dot{X}_2 = -A_1 X_2 + A_2 A_1 \Omega\cos\Omega\tau + A_2\sin\Omega\tau - X_1 + \frac{A_3}{(Z - X_1)^2} - \frac{A_3 A_4{}^6}{30(Z - X_1)^8} \tag{9}$$

with initial conditions of

$$X_1 = 0, \text{ and } X_2 = 0 \tag{10}$$

where $\tau = \omega_t t$, $X_1 = Y_1/Y_s$, $X_2 = Y_2/\omega_t Y_s$, $Z = Z_b/Y_s$, $A_1 = 4/27$, $A_2 = R_m/Y_s$, $A_3 = A_d/Y_s$, $A_4 = c/m_t\omega_t$, $\Omega = \omega/\omega_t$, and (.) denotes the derivative with respect to the normalized time τ.

In the above, X_1 indicates the displacement of the microcantilever tip (where a positive value indicates a displacement towards the sample), X_2 denotes the velocity of the microcantilever tip, and Z is the vibrational amplitude of the dither piezoelectric actuator which drives the tip. Note that both X_1 and Z are non-dimensionalized by the gap between the tip and the sample under equilibrium conditions. In the case where the excitation frequency is close to the natural frequency of the microcantilever, $\Omega = 1$.

Differential transformation is one of the most widely used of all techniques for solving differential equations due to its rapid rate of convergence and its minimal computational error. Furthermore, compared to the integral transformation approach, differential transformation has the further advantage that it can be used to solve nonlinear differential equations. In order to calculate the system equations, differential transformation (DT) method is used and it is one of the most widely used techniques for solving both linear and nonlinear differential equations due to its rapid convergence rate and minimal calculation

error. The basic principles of the DT method approach can be summarized as follows:

Let $P(t)$ be analytic in the time domain T. Furthermore, let

$$Q(t,k) = \frac{d^k P(t)}{dt^k}, \quad \forall t \in T \tag{11}$$

At time $t = t_i$, $Q(t,k) = Q(t_i,k)$, where k belongs to a set of non-negative integers, denoted as the K domain. Therefore, Eq. (11) can be rewritten as

$$\overline{P}_i(k) = Q(t_i,k) = \left[\frac{d^k P(t)}{dt^k}\right]_{t=t_i}, \quad \forall k \in K \tag{12}$$

where $\overline{P}_i(k)$ represents the spectrum of $P(t)$ at $t = t_i$ in the K domain.

If $P(t)$ is analytic in the time domain T, then $P(t)$ can be represented as

$$P(t) = \sum_{k=0}^{\infty} \frac{(t-t_i)^k}{k!} \overline{P}(k) \tag{13}$$

Note that this equation represents the inverse transformation of $\overline{P}(k)$. If $\overline{P}(k)$ is defined as

$$\overline{P}(k) = M(k)\left[\frac{d^k q(t)P(t)}{dt^k}\right]_{t=t_0}, \text{ where } k = 0,1,2,\ldots,\infty \tag{14}$$

then the function $P(t)$ can be expressed as

$$P(t) = \frac{1}{q(t)} \sum_{k=0}^{\infty} \frac{(t-t_i)^k}{k!} \frac{\overline{P}(k)}{M(k)} \tag{15}$$

where $M(k) \neq 0$ and $q(t) \neq 0$. Here, $M(k)$ is a weighting factor and $q(t)$ is a kernel corresponding to $P(t)$. If $M(k) = 1$ and $q(t) = 1$, then Eqs. (12) and (14) and Eqs. (13) and (15) are equivalent. In the analyses performed in this study, the differential transformation operation is performed with $M(k) = \tilde{H}^k/k!$ and $q(t) = 1$, where $\tilde{H}$ is the time horizon of interest. $\overline{P}(k)$ is given by

$$\overline{P}(k) = \frac{\tilde{H}^k}{k!}\left[\frac{d^k P(t)}{dt^k}\right]_{t=t_0}, \text{ where } k = 0,1,2,\ldots,\infty \tag{16}$$

Using DT method, a differential equation in the domain of interest is transformed to an algebraic equation in the K domain and $P(t)$ is given by a finite-term Taylor series plus a remainder, i.e.

$$P(t) = \sum_{k=0}^{n} \left(t - t_0\tilde{H}\right)^k \overline{P}(k) + R_{n+1} \tag{17}$$

In order to accelerate the rate of convergence and improve the accuracy of the calculations, the overall t domain is split into a number of sub-domains and DT method is then used to solve the differential equation in each domain. For example, consider the case in which the time domain is split into a total of n sub-domains. In the first sub-domain (i.e. $0 \leq t \leq t_1, t_0 = 0$), the one-dimensional differential transformation of function $P(t)$is

given by

$$P(t) = \sum_{k=0}^{n} \left(\frac{t-t_0}{\tilde{H}_0}\right)^k \overline{P}_0(k) \tag{18}$$

where $\overline{P}_0(0) = P_0$. Applying the DT method to Eq. (18), the dynamic equation of the system of interest can be solved over the entire period spanned by the first sub-domain. The end point of function $P(t)$ in the first sub-domain is P_1. Furthermore, t has a value of $\tilde{H}_0$. Therefore, $P_1(t)$ is obtained as

$$P_1 = P\left(\tilde{H}_0\right) = \sum_{k=0}^{\infty} \overline{P}_0(k) \tag{19}$$

Note that P_1 represents the initial condition for the second sub-domain and therefore $\overline{P}_1(0) = P_1$. The function $P(t)$ can be expressed in the second sub-domain as

$$P_2 = P(\tilde{H}_1) = \sum_{k=0}^{\infty} \overline{P}_1(k) \tag{20}$$

In general, the function $P(t)$ can be expressed in the $(i-1)$th sub-domain as

$$P_i = P_{i-1} + \sum_{k=1}^{\infty} \overline{P}_{i-1}(k) = \overline{P}_{i-1}(0) + \sum_{k=1}^{\infty} \overline{P}_{i-1}(k), = 1, 2, 3, \ldots\ldots n \tag{21}$$

Using the T spectra method described above, function $P(t)$ can be solved throughout the entire domain.

Table 1 summarizes the principal differential transformation operations in the K domain, where the symbol "^" denotes the differential operator and "⊗" denotes the convolution operation.

Assume that $f(t)$ and $g(t)$ are two uncorrelated functions of t, and that $F(k)$ and $G(k)$ are the corresponding transformation functions, respectively. The basic properties of the DT method approach can be summarized as follows:

1. Linearity: If $F(k) = D[f(t)]$, $G(k) = D[g(t)]$, and C_1 and C_2 are independent of t and k, then

$$D[C_1 f(t) + C_2 g(t)] = C_1 F(k) + C_2 G(k) \tag{22}$$

Table 1
Operation in the K domain with $M(k) = \tilde{H}^k/k!$, $q(t) = 1$.

Operator	
Spectrum $X(k)$	$X(k) = \frac{\tilde{H}^k}{k!}\left(\frac{\partial^k x(t)}{\partial t^k}\right)_{t=0}$
Function $x(t)$	$x(t) = \sum_{l=0}^{k}\left[X(k)\left(t\tilde{H}\right)^k\right]$
Convolution	$X(k) \otimes Y(k) = \sum_{l=0}^{k} X(l)\,Y(k-l)$
Derivative	$(k) = k+1\tilde{H}X(k+1)$

2. Convolution: If $z(t)=f(t)g(t)$, $f(t)=D^{-1}[F(k)]$ and $g(t)=D^{-1}[G(k)]$, then

$$D[z(t)] = D[f(t)g(t)] = F(k) \otimes G(k) = \sum_{l=0}^{k} F(l)G(k-l) = \sum_{l=0}^{k} F(k-l)G(l) \tag{23}$$

Therefore, the differential transform of $f^m(t)$, where m is a positive integer, is obtained as

$$D[f^m(t)] = F^m(k) = F^{m-1}(k) \otimes F(k) = \sum_{l=0}^{k} F^{m-1}(l)F(k-l) \tag{24}$$

3. Derivative: If $f(t)$ and its derivatives $f'(t), f''(t), \ldots, f^{(n)}(t)$ are continuous functions for the interval $[0, \tilde{H}]$, then

$$D\left[\frac{d^n f(t)}{dt^n}\right] = \frac{(k+1)(k+2)\ldots(k+n)}{\tilde{H}^n} F(k+n) \tag{25}$$

In solving Eqs. (8) and (9) using the differential transformation method, the AFM system model is transformed with respect to the time domain τ, and hence the equation becomes

$$\frac{k+1}{H}\overline{X}_1(k+1) = \overline{X}_2(k) \tag{26}$$

and

$$\frac{k+1}{H}\overline{X}_2(k+1) = -A_1\overline{X}_2(k) + A_2A_1\Omega\frac{(\Omega H)^k}{k!}\cos\left(\frac{\pi k}{2}\right) + A_2\frac{(\Omega H)^k}{k!}\sin\left(\frac{\pi k}{2}\right) - \overline{X}_1(k) + \frac{A_3}{(1-\overline{X}_1(k))^2} - \frac{A_3A_4{}^6}{(1-\overline{X}_1(k))^8} \tag{27}$$

respectively.

3. Results and discussions

3.1. Numerical simulation results

As discussed above, the nonlinear behavior of the AFM tip displacement is analyzed in this study using the differential transformation method. The dynamic behavior of the AFM system is characterized with reference to power spectra, Poincaré maps, maximum Lyapunov exponent plots, and bifurcation diagrams produced using the time-series data for the displacement and velocity of the microcantilever tip. Note that in producing these various plots, the time-series data corresponding to the first 1000 revolutions are deliberately excluded in order to ensure that the results reflect steady-state conditions.

Table 2 compares the results obtained by the DT method and the Runge–Kutta (RK) method for the displacement and velocity of the microcantilever tip at various values of the vibrational amplitude of the dither piezoelectric actuator. It is seen that a good agreement exists between the two sets of numerical results at $H=0.01$. However, the results at $H=0.001$ are still in agreement to approximately 5–6 decimal places compared with $H=0.01$ for DT method and even better than RK method for 2–3 decimal places. From the above results, DT method used for AFM system will be more accurate than RK method. In the following calculation, the DT method is used to calculate and analyze this nonlinear problem.

Table 3 clarifies the effect of the time-step value on the Poincaré maps for the microcantilever tip at different values of the vibrational amplitude via DT method. It can be seen that for a given vibrational amplitude, the tip displacement and velocity values calculated using different values of the time step are in agreement to approximately 5–6 decimal places.

3.2. Phase portraits

As shown in Fig. 2, the phase portraits of the tip displacement at various values of the vibrational amplitude, Z, are non-symmetrical, i.e. the tip exhibits a nonlinear dynamic response. Fig. 2(a–h) reveals that the tip orbit is regular at low values of vibrational amplitude, i.e. $Z=1.344$ and 1.377, but becomes irregular when the vibrational amplitude

Table 2
Comparison of tip displacement and velocity values calculated using DT and RK methods, respectively.

Vibrational amplitude	Time-step numerical method	Tip displacement X_1		Tip velocity X_2	
		$H=0.001$	$H=0.01$	$H=0.001$	$H=0.01$
DT	$Z=1.0$	−0.3334158965	−0.3334159441	0.4364918561	0.4364917483
RK		−0.3330029331	−0.3334228944	0.4361927663	0.4364337922
DT	$Z=1.2$	−0.3550410095	−0.3550411778	0.6575847688	0.6575849077
RK		−0.3552401285	−0.3550409900	0.6532117827	0.6575834245
DT	$Z=1.8$	−0.3976903894	−0.3976904010	1.2893464872	1.2893465263
RK		−0.3988125150	−0.3976324033	1.2876564921	1.2893414772
DT	$Z=2.1$	−0.4233235901	−0.4233237384	1.5976025975	1.5976016639
RK		−0.4256219173	−0.4233265923	1.5903005645	1.5976025729

Table 3
Comparison of Poincaré maps of tip displacement and velocity at different values of time step, H via DT method.

$Z=2.3$			$Z=2.48$		
H	X_1(nT)	X_2(nT)	H	X_1(nT)	X_2(nT)
π/200	−0.4436110921	1.8014718981	π/200	−0.4642972668	1.9840682627
π/400	−0.4436196085	1.8014721059	π/400	−0.4642911344	1.9840617022
π/800	−0.4436194437	1.8014782723	π/800	−0.4642975571	1.9840627282

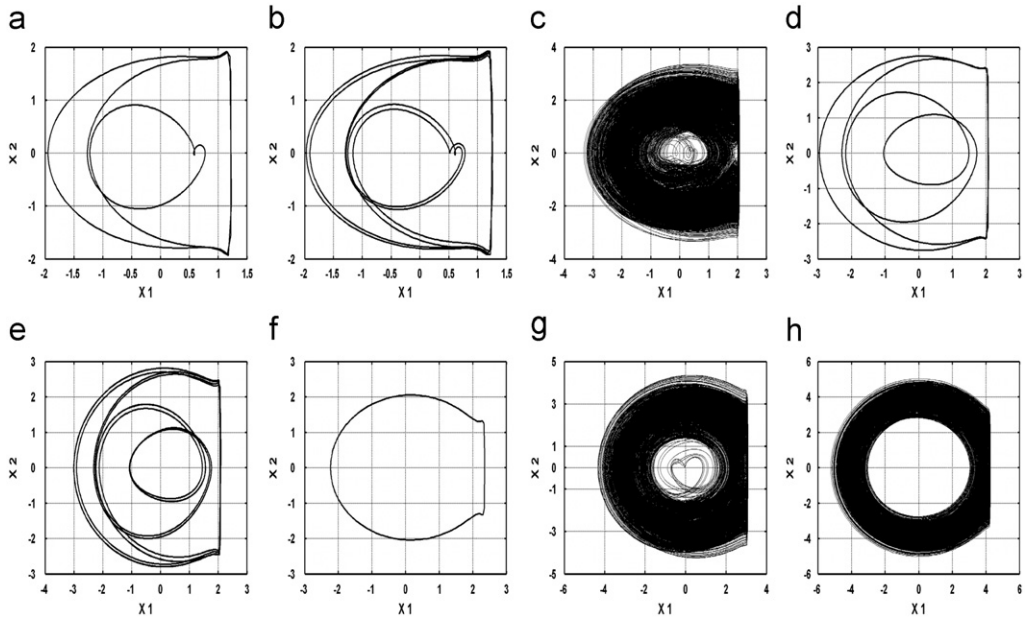

Fig. 2. Phase portraits of microcantilever tip at $Z=1.344$, 1.377, 2.172, 2.183, 2.198, 2.48, 3.185, and 4.36.

is increased to $Z=2.172$. However, when the vibrational amplitude is increased further to $Z=2.183$, 2.198, and 2.48, the tip orbit exhibits regular and symmetric motions. Then, the tip orbit performs a complex, non-periodic motion at $Z=3.183$ and 4.36.

3.3. Power spectra

Figs. 3(a–h) and 4(a–h) show the dynamic displacement and velocity responses of the microcantilever tip, respectively. At vibrational amplitudes of $Z=1.344$ and 1.377, respectively, the power spectra show that the microcantilever tip performs 3T-subharmonic and 6T-subharmonic motions, respectively. However, when the vibrational amplitude is increased to $Z=2.172$, it can be seen that the tip exhibits chaotic motion. But, the chaos behavior changes to subharmonic motions at $Z=2.183$, 2.198, and 2.48. Finally, at vibrational amplitudes of $Z=3.183$ and 4.36, respectively, the tip has a chaotic behavior.

3.4. Maximum Lyapunov exponent

The maximum Lyapunov exponent can also be used to identify the dynamic behavior of the AFM tip. Fig. 5(a, b, and d–f), corresponding to vibrational amplitudes of $Z=1.344$, 1.377, 2.183, and 2.198, respectively, shows that the maximum Lyapunov exponent has a value of approximately zero, which indicates that the microcantilever tip has a periodic response. However, at $Z=2.172$, 3.183, and 4.36, as shown in Fig. 5(c, g, and h), respectively, the maximum Lyapunov exponent is positive, and hence it can be inferred that the system has a chaotic response.

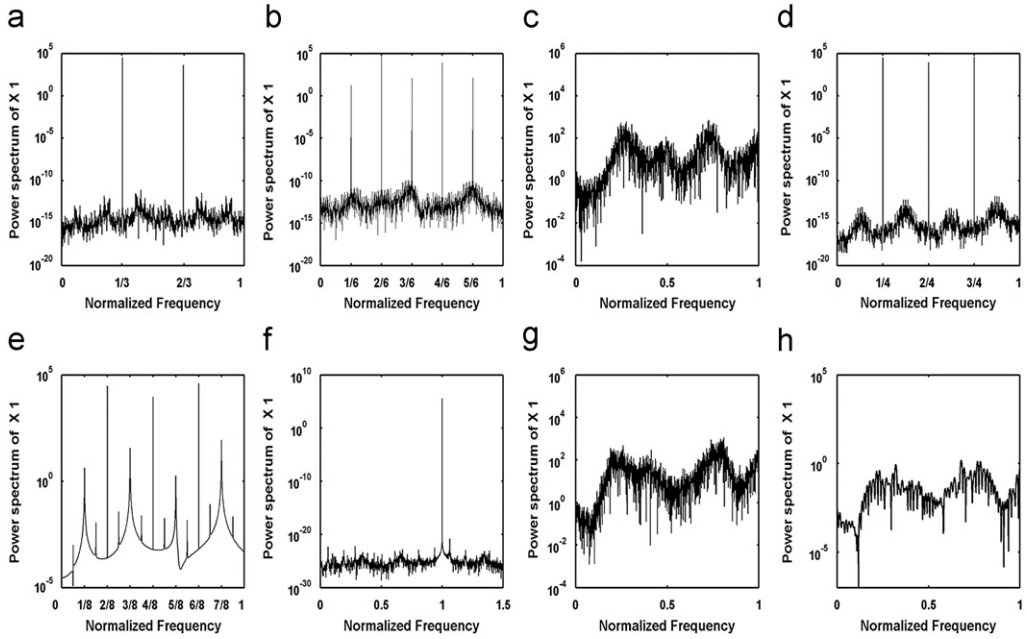

Fig. 3. Power spectra of displacement (X_1) of microcantilever tip at $Z = 1.344$, 1.377, 2.172, 2.183, 2.198, 2.48, 3.185, and 4.36.

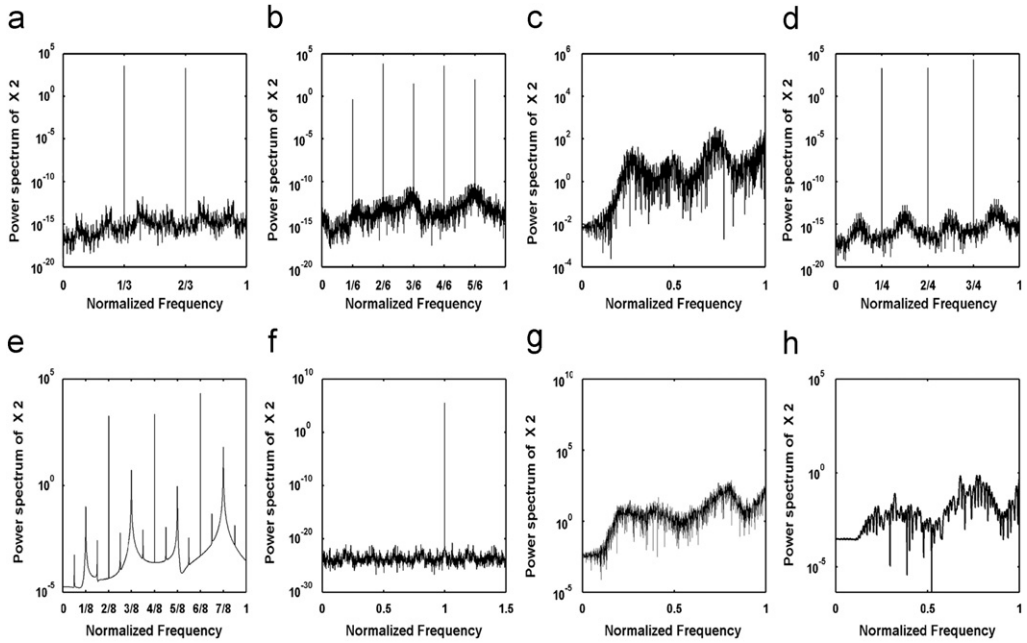

Fig. 4. Power spectra of velocity (X_2) of microcantilever tip at $Z = 1.344$, 1.377, 2.172, 2.183, 2.198, 2.48, 3.185, and 4.36.

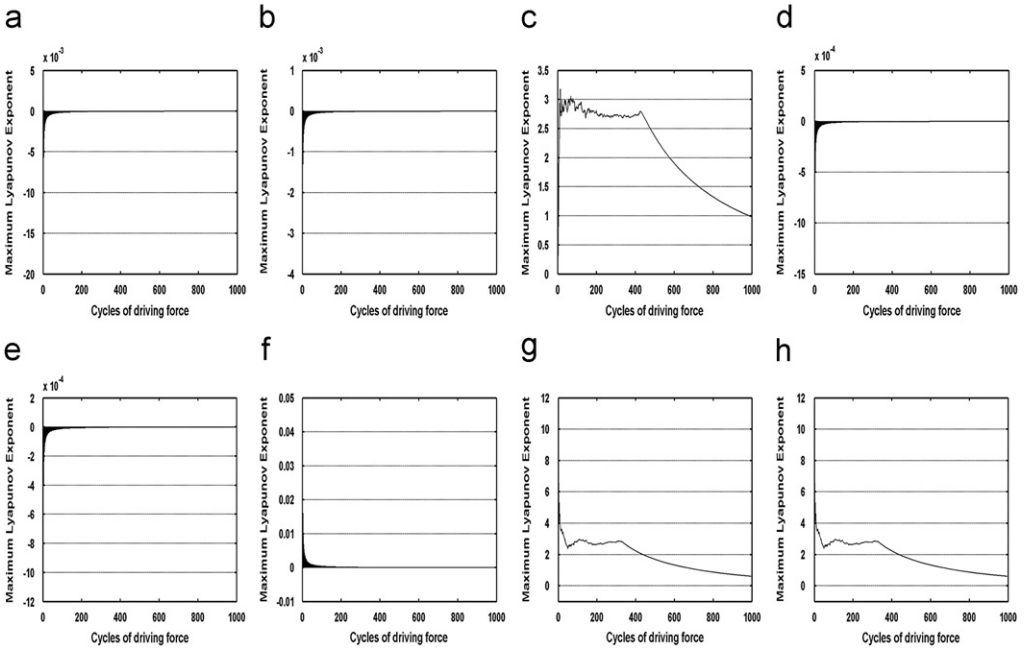

Fig. 5. Maximum Lyapunov exponents of microcantilever tip at different values of vibrational amplitude Z: (a) 1.344, (b) 1.377, (c) 2.172, (d) 2.183, (e)2.198, (f) 2.48, (g) 3.185, and (h) 4.36.

3.5. Bifurcation diagrams and Poincaré maps

In general, bifurcation diagrams and Poincaré maps summarize the essential dynamics of a system, and are therefore useful tools for observing nonlinear dynamic behavior. In the current study, Figs. 6 and 7 plot the bifurcation diagrams of the tip displacement and the tip velocity, respectively, taking the vibrational amplitude (Z) of the cantilever tip as the bifurcation parameter. Finally, Fig. 8(f) presents the Poincaré maps of the microcantilever tip trajectory at $Z=1.344$, 1.377, 2.172, 2.183, 2.198, 2.48, 3.185, and 4.36, respectively.

Figs. 6(b, c) and 7(b, c) show that at lower values of the vibrational amplitude, i.e. $Z<2.172$, the displacement (X_1) and velocity (X_2) of both the tips exhibits a dynamic periodic response, including T-, 3T- and 6T-periodic motions except for the chaotic motions at $Z=1.531$, 1.546, and 1.577. Fig. 8(a and b) presents the Poincaré map corresponding to $Z=1.344$ and 1.377, and the maps have three and six discrete points, which confirm the existence of 3T- and 6T-periodic behavior as shown in the bifurcation diagrams. As the value of the vibrational amplitude is increased from $Z=2.172$ to 2.34, Figs. 6(c) and 7(c) show that both the tip displacement and the tip velocity perform 4 kinds of motions including T-, 4T-, 8T-periodic, and chaotic motions. Fig. 8(c, d, and e) present the Poincaré maps at $Z=2.172$(chaotic), 2.183(4T), and 2.198(8T), respectively. At $Z=2.341$, the T-periodic motion is replaced by chaotic motion, as shown in Figs. 6(c) and 7(c). When Z is increased over the interval $2.341\leq Z<2.883$, the tip response includes both chaotic and T-periodic motion. Fig. 8(f) presents the Poincaré map at $Z=2.48$. However, at $Z=2.883$, the T-periodic motion is replaced by 6T-periodic motion. Thereafter, the

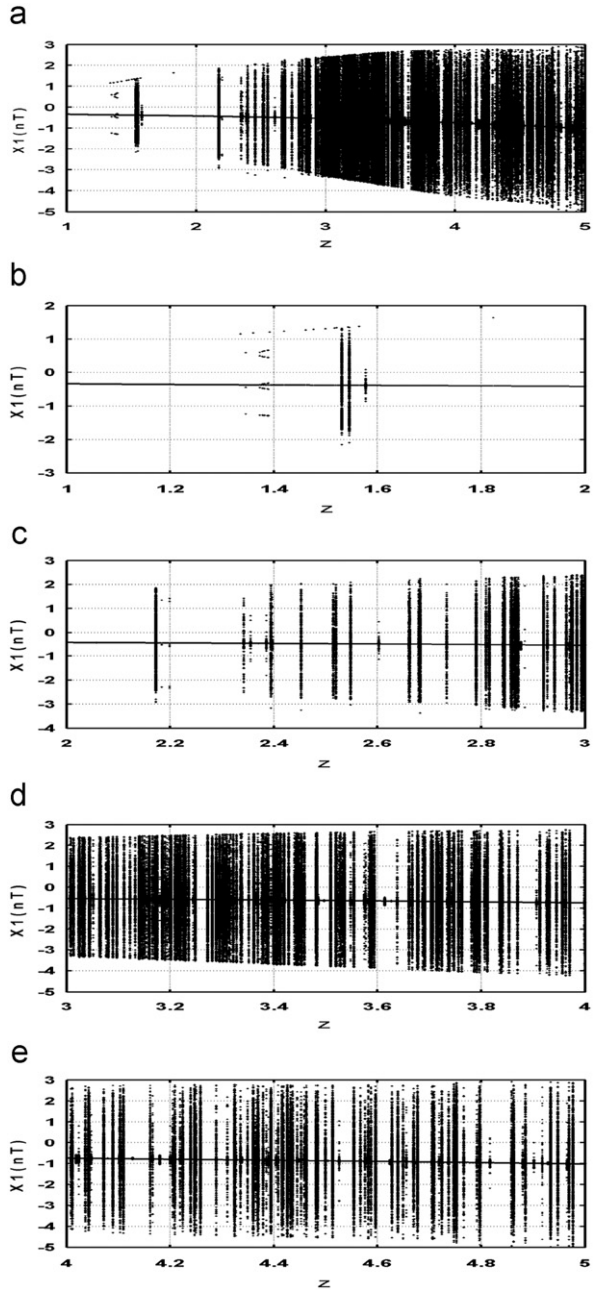

Fig. 6. Bifurcation diagrams for tip displacement using vibrational amplitude (Z) as the bifurcation parameter.

6T-periodic motion changes its stability at $Z=2.884$ and is replaced by T-periodic motion. But for vibrational amplitudes in the range $2.884 \leq Z < 5$, Figs. 6(d, e) and 7(d, e) show that the tip performs both T- and chaotic motions. Fig. 8(g and h) presents the Poincaré maps at $Z=3.185$ and 4.36, respectively.

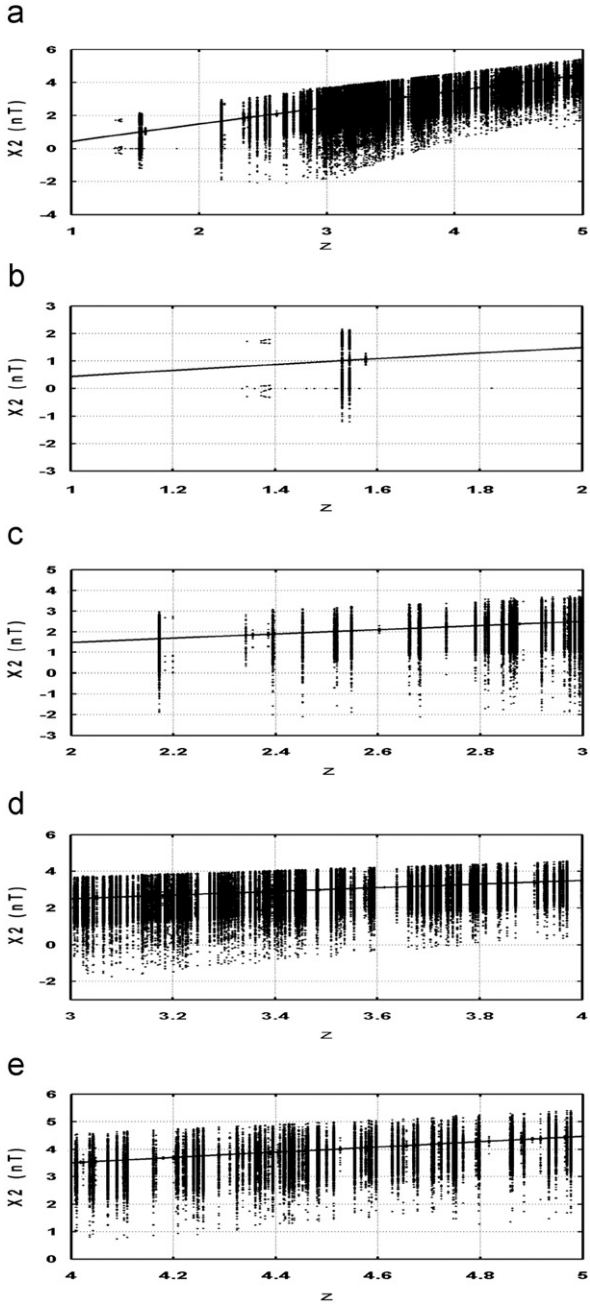

Fig. 7. Bifurcation diagrams for tip velocity using vibrational amplitude (Z) as the bifurcation parameter.

From the discussions above, it is clear that the dynamic response of the probe tip depends on the magnitude of the vibrational amplitude. The various motions performed by the tip as the vibrational amplitude increases from 1.0 to 5.0 are summarized in Table 4. In general, the results show that depending on the value of the vibrational amplitude, the tip

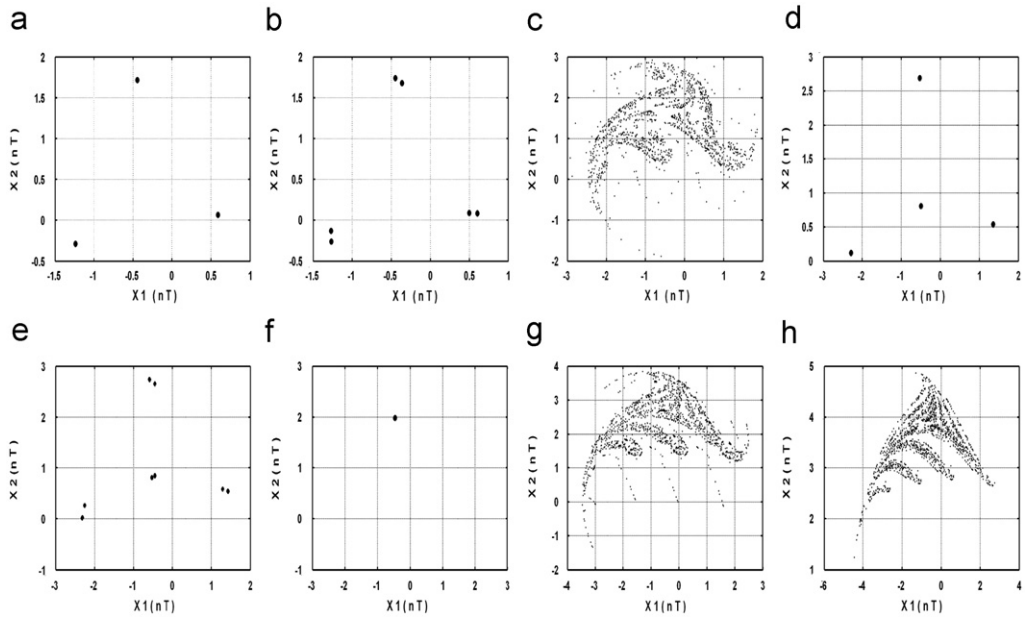

Fig. 8. Poincaré maps of microcantilever tip trajectory at different values of vibrational amplitude (Z): (a) 1.344, (b) 1.377, (c) 2.172, (d) 2.183, (e) 2.198, (f) 2.48, (g) 3.185, and (h) 4.36.

Table 4
Variation of microcantilever tip response with vibrational amplitude over interval $1.0 \leq Z' \leq 5.0$ via DT method.

Z	[1.0, 1.344]	[1.344,1.578]	[1.578,2.172]	[2.172,2.2]	[2.883]	[2.2,5]
Dynamic behavior	T	T,3T,6T,chaos	T	T,4T,8T,chaos	5T	T,chaos

may exhibit periodic behavior, i.e. T-, 3T- or 6T-periodic motion or multi-periodic, or a chaotic response. This result also indicates that a discontinuous increase takes place in the size and form of the chaotic attractor as the vibrational amplitude is increased.

4. Conclusion

In the present paper the nonlinear dynamics of a microcantilever in the AFM system has been studied and applied to the differential transformation method and the Runge–Kutta method, respectively, to investigate the non-periodic behaviors and nonlinear equations. Phase trajectories, Poincaré maps, maximum Lyapunov exponent plots, and bifurcation diagrams have been used to characterize the dynamic response of the microcantilever as a function of the tip's vibrational amplitude and to detect the occurrence of chaotic motion. In general, the results have shown that as the vibrational amplitude is increased from 1.0 to 5.0, the microcantilever tip motion changes initially from T-periodic to 3T-periodic, and then from 6T-periodic to multi-periodic, and finally to chaotic motion with windows of periodic motion.

Acknowledgment

The financial support provided to this research by the National Science Council of the R.O.C. under Grant no. NSC-95-2221-E-269-016 is greatly appreciated.

References

[1] M. Goeken, M. Kempf, Microstructural properties of super alloys investigated by nanoindentations in an atomic force microscope, Acta Materialia 47 (1999) 1043–1052.
[2] N. Nagashima, S. Matsuoka, K. Miyahara, Nanoscopic hardness measurement by atomic force microscope, JSME International Journal Series A: Mechanical Material Engineering 39 (1996) 456–462.
[3] N.A. Burnham, A.J. Kulik, G. Germaud, G.A.D. Briggs, Nanosubharmonics: the dynamics of small nonlinear contacts, Physical Review Letters 74 (1995) 5092–5095.
[4] M. Ashhab, M. Salapaka, M. Dahleh, I. Mezic, Melnikov-based dynamical analysis of microcantilevers in scanning probe microscopy, Nonlinear Dynamics 20 (1999) 197–220.
[5] A. Sebastian, M. Salapaka, D. Chen, J. Cleveland, Harmonic analysis based modeling of tapping-mode AFM, in: Proceedings of the American Control Conference, San Diego, CA, 1999, pp. 232–236.
[6] M. Basso, L. Giarre, M. Dahleh, I. Mezic, Numerical analysis of complex dynamics in atomic force microscopes, in: Proceedings of the IEEE Conference on Control applications, Trieste, Italy, 1998, pp. 1026–1030.
[7] S.I. Lee, S.W. Howell, A. Raman, R. Reifenberger, Nonlinear dynamic perspectives on dynamic force microscopy, Ultramicroscopy 97 (2003) 185–198.
[8] S. Ruetzel, S.I. Lee, A. Raman, Nonlinear dynamics of atomic-force-microscope probes driven in Lennard–Jones potentials, Proceeding of Royal Society of London A 459 (2003) 1925–1948.
[9] J.J. Yan, M.L. Hung, J.S. Lin, T.L. Liao, Controlling chaos of a chaotic nonlinear gyro using variable structure control, Mechanical Systems and Signal Processing 21 (2007) 2515–2522.
[10] H.T. Yau, Chaos synchronization of two uncertain chaotic nonlinear gyros using fuzzy sliding mode control, Mechanical Systems and Signal Processing 22 (2008) 408–418.
[11] C.C. Wang, H.T. Yau, Application of a hybrid numerical method to the bifurcation analysis of a rigid rotor supported by a spherical gas journal bearing system, Nonlinear Dynamics 51 (2008) 515–528.
[12] N. Jalili, K. Laxminarayana, A review of atomic force microscopic imaging systems: application to molecular metrology and biological sciences, International Journal of Mechatronics 14 (2004) 907–945.
[13] N. Jalili, M. Dadfarnia, D.M. Dawson, A fresh insight into the microcantilever–sample interaction problem in non-contact atomic force microscopy, ASME Journal of Dynamic System, Measure Control 126 (2004) 327–335.
[14] M. Ashhab, M. Salapaka, M. Dahleh, I. Mezic, Dynamical analysis and control of microcandilevers, Automatica 35 (1999) 1663–1670.